

Asbjørn Bjørkkjær

Exploring 7T GluCEST MRI Techniques for Mapping Neurometabolism

A novel approach to increase low-level glutamate contrast

Project thesis in Electronic System Design and Innovation

Supervisor: Dag Roar Hjelme

Co-supervisors: Jin Li, Axel Karl Gottfried Nyman

December 2024

Norwegian University of Science and Technology

Faculty of Information Technology and Electrical Engineering

Department of Electronic Systems



Abstract

The human brain contains almost a hundred billion neurons and the majority of synapses in the cortex (80-90%) are glutamatergic.^[1] The dysfunction and loss of synapses contribute to neurodegenerative disorders, with accumulation of tau proteins in dementia strongly associated with loss of glutamate. This glutamate metabolic impairment can start years before detectable changes using conventional structural brain imaging. Glutamate-weighted chemical exchange saturation transfer (GluCEST) magnetic resonance imaging (MRI) allows non-invasive imaging of glutamate metabolites in the brain. This novel imaging method can be explored to assess neurological disorders' pathophysiology, development, and early stages of diseases such as Huntington's and Alzheimer's.

GluCEST imaging on phantoms of ranged glutamate concentrations was acquired on a *Bruker 7T BioSpec* scanner. A GluCEST protocol of 10 binomial pulses was employed, using B_1 pulses of $3 \mu T$ and 3 s saturation time as a baseline. Z-spectrums were obtained from 5 ppm to -5 ppm with 50 frequency offsets (step size 0.2) and normalized with an unsaturated scan at -100 ppm.

The GluCEST effect in the most promising acquisition, using saturation time of 3 s and a pulse power of $2 \mu T$ with shimming, yielded an $MTR_{\text{asym}} = 5.22 \pm 0.06 \%$ in the solution with 10 mM of glutamate. There was a linear proportional dependency of GluCEST effects on the glutamate concentration. Another acquisition of $4 \mu T$ without shimming resulted in a higher GluCEST contrast of $MTR_{\text{asym}} = 10.79 \pm 0.08 \%$, although it showed less linear dependency. GluCEST can thus be used for non-invasively mapping neurometabolism and will assist the research of neurodegenerative disorder development.

Acknowledgements

This work is partly funded by NTNU by the MR Core Facility and St. Olavs Hospital by the project led by postdoc and medical doctor Axel Karl Gottfried Nyman from K.G. Jebsen Centre for Alzheimer's Disease (JCA) and NTNU.

Moreover, the Cancer Imaging and Multi-Omics Research Group (CIMORe) at St. Olavs Hospital has provided an office and a community for the project to be comprehensively explored. The CEST research group in FAU Erlangen-Nürnberg (Germany), in addition to PhD students from Harvard University (USA) and Toronto Metropolitan University (Canada), have supported the work with efficient pipelines for post-processing and calculations for the GluCEST effects.

Thanks to Dag Roar Hjelme and Jin Li (NTNU), Axel Nyman (JCA, NTNU), Moritz Zaiß and Moritz Simon Fabian (FAU), David Korenchen (Harvard), and Siddhart Sadanand (Toronto) for invaluable help throughout the first project phase.

Contents

Abstract	i
Acknowledgements	ii
Contents	iii
List of Figures	v
List of Tables	vi
Abbreviations	vii
1 Introduction	1
1.1 Motivation	2
1.2 Project description	3
2 The Seamless Integration of CEST in MRI	5
Introduction to Nuclear Magnetic Resonance	5
2.1 Magnetic Precession	5
2.2 Magnetic Resonance	6
2.3 Magnetic Resonance Spectroscopy	8
2.4 Magnetic Resonance Imaging	10
2.5 Chemical Shift	12
Introduction to chemical exchange saturation transfer	12
2.6 Adding Molecular Information to MRI	13
2.7 Controlled CEST Sequences	15
2.8 Fitting the Z-spectrum	16
2.9 Artifacts in MRI	17

3	Methodology	19
3.1	Phantom preparation	19
3.2	GluCEST experiment	20
3.3	Post-processing	21
4	Results of the GluCEST MRI	23
4.1	GluCEST contrast enhancement	23
4.2	Artifacts	32
5	Discussion	33
5.1	GluCEST contrast variations	33
5.2	Future work	34
6	Conclusion	37
	Appendices:	41
A	Github repositories	42
B	Declaration of AI aids and -tools	43

List of Figures

2.1.1 Precessing	6
2.2.1 Net magnetization	7
2.3.1 Free induction decay	8
2.3.2 Relaxation of T_1 and T_2	9
2.3.3 T_R and T_E	10
2.4.1 Filling the k-space	11
2.5.1 The basics of CEST	13
2.6.1 MRS spectrum	13
2.6.2 Z-spectrum	14
2.7.1 Pulsed CEST setup	15
2.7.2 Binominal pulses	16
2.8.1 Z-spectrum calibration	16
2.9.1 MRI scan	17
2.9.2 MRI scan with artifact	17
3.1.1 Phantom preparation	20
4.1.1 T2W localizer	24
4.1.2 B_0 map	24
4.1.3 GluCEST 300ms 3uT	25
4.1.4 GluCEST 200ms 3uT	26
4.1.5 GluCEST 300ms 2uT	27
4.1.6 GluCEST 300ms 4uT	28
4.1.7 GluCEST 100ms 3uT	29
4.1.8 GluCEST 300ms 2uT	30
4.1.9 Linear dependency in MTR_{asym}	31

List of Tables

3.1.1 Prepared GluCEST concentrations	19
3.2.1 Details of the CEST sequences	21
4.1.1 MTR_{asym} for acquisition 1	25
4.1.2 MTR_{asym} for acquisition 2	26
4.1.3 MTR_{asym} for acquisition 3	27
4.1.4 MTR_{asym} for acquisition 4	28
4.1.5 MTR_{asym} for acquisition 5	29
4.1.6 MTR_{asym} for acquisition 6*	30

Abbreviations

List of all abbreviations in alphabetic order:

- **APT** Amide proton transfer
- **CEST** Chemical exchange saturation transfer
- **CNR** Contrast-to-noise ratio
- **DS** Direct water saturation
- **FOV** Field of view
- **Glu** Glutamate
- **MALDI-MSI** MALDI mass spectroscopy imaging
- **MRI** Magnetic resonance imaging
- **MTR** Magnetization transfer ratio
- **MTR_{asym}** Asymmetric magnetization transfer ratio
- **PBS** Phosphate-buffered saline water
- **ROI** Region of interest
- **SEM** Standard error of the mean
- **SNR** Signal-to-noise ratio

Introduction

Magnetic resonance imaging (MRI) is a non-invasive imaging technique mostly used to acquire information about soft tissues in the human body. The key concept is to initiate a strong magnetic field to excite ^1H protons so they start precessing. This precession can be measured, revealing the tissue from which the proton originates. By tailoring the magnetic pulse sequences to the tissue of interest, MRI can exhibit vital images of the body - especially in the brain due to its abundance of water molecules. Clinically, brain MRI reveals critical details about various brain tumors, lesions, or signs of dementia, among other conditions.

Moreover, by employing chemical exchange saturation transfer (CEST), one can additionally obtain metabolic information that is associated with, for example, tumor aggressiveness and stages of dementia - features that are not shown in regular MRI scans. CEST is a type of MRI that utilizes the chemical exchange of ^1H between pools of low-concentrated metabolites and water within a region. After some time, these chemical exchanges will saturate and lead to a decreased water signal. This method indirectly detects the concentration of the relevant metabolite, which can be localized and quantified in an MRI scan.

All these wonders are achievable by concerning the magnetic fields and designing the CEST pulse sequences with intentional care. The foundation of MRI is well phrased by Nikola Tesla (1856-1943):

If you want to find the secrets of the universe, think in terms of energy, frequency, and vibrations. (N. Tesla)

1.1 Motivation

There are unmet needs in the field of neurometabolism today regarding the development of neurodegenerative disorders. The dysfunction and loss of synapses are contributing factors for such disorders, and most of them start with a cognitive dysfunction without evidence of detectable macroscopic structural change. Furthermore, the accumulation of tau proteins associated with cognitive dysfunction is strongly associated with memory loss and loss of glutamate. This biochemical evolution of the human brain can be seen years before structural brain imaging can detect signs of diseases.^[1] This suggests that glutamate-weighted CEST (GluCEST) can be used to search for neurological disorders' pathophysiology, development, and early stages of diseases such as Huntington's and Alzheimer's.

There are acquisition modalities in conventional MRI to image anatomical structures of the brain, but the implementation of CEST is yet an esoteric field clinically. One challenge is the time needed for each scan. Regular MRI typically requires 30-40 min for a brain scan. The CEST MRI is further recognized as a time-consuming acquisition modality that needs additional scan time, which makes it inconvenient to add to a clinical scanning program. Another challenge is the factors that contribute to GluCEST effects. Unknown pools of metabolites, and changing temperature and pH, especially for measurements *in vivo*, are all parameters that can distort and falsify CEST images. Additionally, CEST signals are proportional to magnetic field strengths, which means that a higher magnetic field yields better image contrast. The lack of scanners with high field strengths ($\geq 7\text{T}$) is, consequently, one of the problems in spreading CEST MRI to all the clinics.

There have been several studies to increase the contrast and reduce the acquisition time in GluCEST and CEST MRI in general. Cai et al. (2012) have compared GluCEST *in vitro* and *in vivo*, observing differences in the GluCEST signal between phantoms and rodents. Zaiß et al. (2022) have investigated the impact of different magnetic fields and radiofrequency (RF) bandwidths. Another attempt has been to obtain CEST signals using continuous wave saturation pulses (Simegn et al. 2020). However, there is still plenty of room for improvement - the acquisition time is noticeably long, and the contrast can often be improved. These challenges, among others, will be explored in this thesis.

1.2 Project description

The project aims to determine whether GluCEST reflects the true glutamate concentration within solutions of ranging concentrations. This will be evaluated by exploring the contrast between six GluCEST pulse sequences on a 7T pre-clinical scanner. The baseline for this project is the phantom study *in vitro* examined by Cai et al. (2012), and a variety of magnetic field strengths will be tested, similar to what Zaiß et al. (2022) did. The goal is to implement a working GluCEST MRI pipeline and explore variables that contribute to GluCEST effects.

The Seamless Integration of CEST in MRI

Understanding the principles of MRI is crucial to making use of CEST. It is needed such that the metabolic information and contrast enhancement can be properly utilized. MRI can be well examined using the historical line of innovations through the 20th century. Starting with Stern in 1922, through Rabi and Bloch in 1937 and 1946, respectively, and ending with Ernst, Lauterbur, and Mansfield in the 60s and 70s, all the necessary parts needed to grasp the basics of magnetic resonance can be understood. For clarity, the theory part will explain nuclear magnetic resonance (NMR), where some derivations and images are adopted from Suetens^[2] and Webb^[3]. Later, NMR will be used to obtain an image that leads to MRI.

Introduction to Nuclear Magnetic Resonance

NMR can be explained by its acronym: achieving resonance of nuclei using magnetism. Nuclei have magnetic properties, so-called spins, which can be affected by an external magnetic field. The attention of spins is normally in the ^1H due to its simplicity of having only one proton. In light of the probabilistic nature of electrons, considerations of the wave function should be present when dealing with spins. It has been argued, however, that it is possible to treat NMR without quantum physics.^[2] Using a mechanical view is, thus, sufficient to explain the basic principle of magnetic resonance and to understand it more intuitively.

2.1 Magnetic Precession

The magnetic properties, hereafter referred to as spins, of ^1H protons were first discovered by Otto Stern in 1922. He found that the spins will respond depending on their quantum state.^[2] If we treat the protons as either spin-up or spin-down, and consider them a sphere with an axial precession, it is possible to elaborate with a mechanical treatment.

Using the angular velocity $\vec{\omega}$ of spins, hereby referred to as the frequency of spins, in a magnetic field \vec{B} , their precessing motion can be visualized as shown in figure 2.1.1.

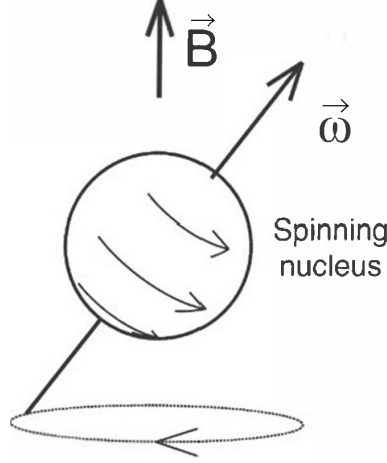


Figure 2.1.1: A proton that undergoes precession with angular velocity $\vec{\omega}$ in an external magnetic field \vec{B} . Adopted from [4].

Introducing the resonance frequency of the precessing motion, ω_0 , known as the *Larmor frequency*, its relation to \vec{B} can be derived.^[2] Letting \vec{B} be a static field in \hat{z} -direction, $\vec{B} = B_0 \cdot \vec{e}_z$, the relation to the precession motion is given by the following equation, called the *Larmor equation*

$$\omega_0 = \gamma B_0. \quad (2.1)$$

The gyromagnetic ratio γ is the ratio of the magnetic moment to angular velocity, which for ^1H protons is $42.58 \frac{\text{MHz}}{\text{T}}$. This equation is pivotal in NMR as it establishes the strength of B_0 with the Larmor frequency. It has to be emphasized that this is still a classical treatment of isolated spins. However, treating the protons as precessing objects, one can use the Larmor equation in (2.1) without any quantum physics.

2.2 Magnetic Resonance

To this point, protons in the main external magnetic field B_0 , hereby denoted without vectors, will undergo precession, either aligned with the field in \hat{z} -direction as spin-up or in the opposite direction as spin-down. In this equilibrium state, nothing particular will happen. Introducing an additional radiofrequency (RF) pulse B_1 , close to the Larmor frequency, the precessing protons will be

driven into resonance. This effect, discovered by Isaac Rabi in 1937, is the contributing factor that makes the signal from the spins detectable.

Alone, a single spin cannot be detected when it undergoes resonance. In a medium, however, when there are many ^1H closely spaced, the spins can be added together which sums up to a net quantity of spins. This is called the net magnetization vector \vec{M} . Due to a lower energy level for a precessing proton with spin-up, there will be a slight net of spins in the direction of B_0 . For example, the number of excess spin-up in $B_0=1\text{T}$ is approximately 6 spins per million spins.^[6] Those six spins are, however, enough to undergo resonance and generate a detectable signal. In equilibrium, when only B_0 is present, the $\vec{M} = M_z \cdot \vec{e}_z$ will be oriented along this direction. The net magnetization M_z is given in a macroscopic view and is typically the quantity that is referred to when considering spins.

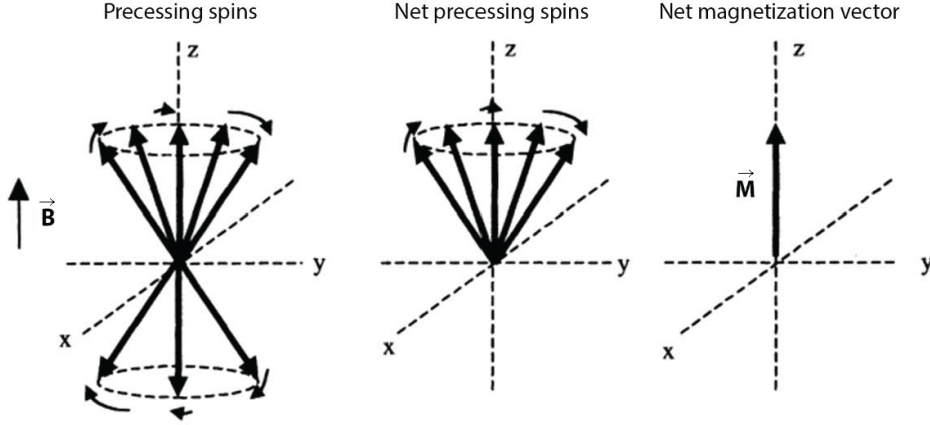


Figure 2.2.1: The net magnetization vector \vec{M} is the macroscopic view on the net amount of spins. Its components in \hat{z} -direction and in the xy -plane are denoted M_z and M_{xy} , respectively. Adopted from [3].

In 1947, Felix Bloch experimented with the magnetic resonance of protons in mediums, showing that this method could be utilized in samples and tissues. Applying an RF pulse, also known as the B_1 pulse, with the same frequency as the Larmor frequency, the spins will be driven into resonance such that \vec{M} are precessing in the xy -plane. Furthermore, after the RF pulse is applied, \vec{M} will have a relaxation time back to equilibrium. This time depends on the type of medium the spins are coming from, e.g. spins in water will relax slower than spins in fat. Owing to this, Bloch deduced equations describing the rate of change of \vec{M} in \hat{x} , \hat{y} , and \hat{z} -direction with the matrix system

$$\frac{d\vec{M}(t)}{dt} = \vec{M}(t) \times \gamma \vec{B}_0(t). \quad (2.2)$$

This fact reveals that the components of \vec{M} provide intrinsic information of the medium wherein the spins are. In other words, measuring the components of \vec{M} allows us to find what type of medium the spins originate from.

2.3 Magnetic Resonance Spectroscopy

The relaxation process is detected using coils placed close to the medium. The spins in resonance, all acting as small magnets, will induce a current in the coils. This is maintained by inserting a 90° RF pulse such that the net magnetization M_z is flipped orthogonally on \hat{z} down to the xy -plane. This yields a detectable signal, known as free induction decay (FID), illustrated in figure 2.3.1.

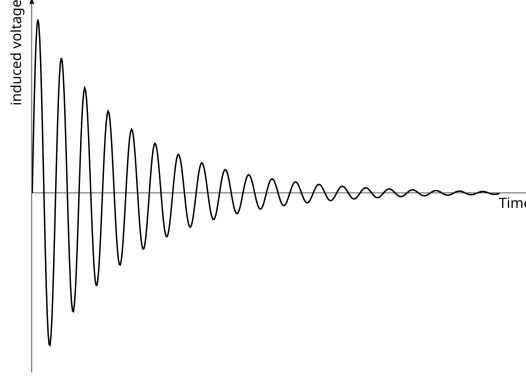


Figure 2.3.1: Free induction decay is the signal from the relaxing magnetization vector \vec{M} back to equilibrium. Adopted from [5].

The FID signal displays the response of the spins in resonance, which, in turn, is characterized by the medium they originate from. In the 60s, while the Fourier transform was increasingly used, Richard Ernst explored how FID signals could be interpreted regarding frequencies. Ernst found in 1966 that the frequency content of the FID signal is related to spins from different types of mediums.^[3] This observation led to magnetic resonance spectroscopy (MRS), which plays a crucial role in CEST.

The decay of the FID signal, given by the relaxation time of \vec{M} , can be utilized for two simplified measurements: the imaging modalities of T_1 and T_2 . These quantities are related to the decay of M_z and M_{xy} , respectively. T_1 yields how fast the M_z component is recovered, while T_2 measures how fast the M_{xy} component is lost. This can be thoroughly understood using figure 2.3.2.

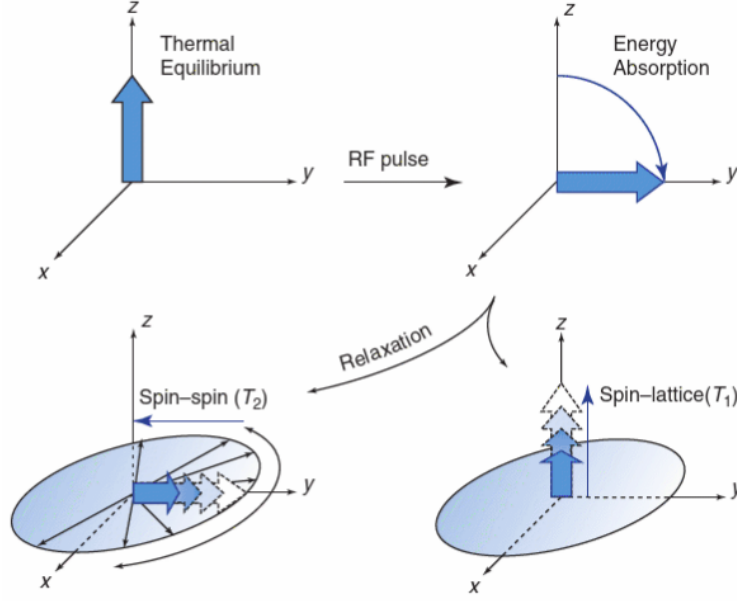


Figure 2.3.2: The evolution of T_1 and T_2 after a 90° pulse.^[2]

The different modalities using T_1 and T_2 are especially important when distinguishing wet tissues. Water and fat, for example, have different T_1 and T_2 values. As a result, they induce image contrast and are hence distinguishable in the images.

T_1 and T_2 are intrinsic values related to the medium of interest, i.e. that cannot be changed. Delving into the equations of how the FID signal is measured, it is possible to change other parameters to indirectly change T_1 and T_2 . It can be shown^[2] that the FID signal is given by

$$\text{FID} = M_0 \cdot (1 - e^{-\frac{T_R}{T_1}}) \cdot \cos(\omega_0 t) \cdot e^{-\frac{t}{T_2^*}} \quad (2.3)$$

where T_R and $t=T_E$ are the repetition and echo time, respectively. Note that $T_2 \neq T_2^*$, whereas T_2 is the intrinsic value of relaxation and T_2^* is the measured quantity.^[2] The relaxation times using T_R and T_E can be better understood in figure 2.3.3.

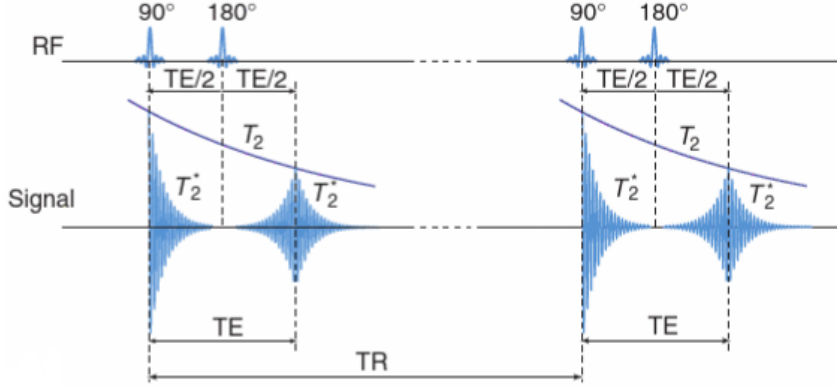


Figure 2.3.3: The relation between the echo time T_E and repetition time T_R . The FID signal decays with T_2^* after the pulse of 90° . The inversion pulse of 180° makes the spins recover to the intrinsic value of the T_2 decay, which increases the detected signal. Adopted from [2].

As displayed in figure 2.3.3, T_R yields the time between each 90° RF pulse. On the other hand, T_E is the time between the 90° RF pulse and the readout of the FID, i.e. the time for the spins to relax before detection. An inversion pulse of 180° is applied for the spins to be inverted and effectively recover their components. In this way, the detected signal will be increased.^[2] By carefully determining T_R and T_E , the contribution of the intrinsic values T_1 and T_2 can be changed.

2.4 Magnetic Resonance Imaging

At this point, the precessing protons are aligned with B_0 and can be excited by an RF pulse. Finally, the relaxation back to equilibrium can be detected as the FID signal in the coils. Still, there are yet no images. Images are calculated similarly to computed tomography.^[2] There are, however, special techniques needed to utilize the power of MRI. These findings were discovered throughout the 70's by Paul Lauterbur and Peter Mansfield.

Firstly, the RF pulse needs to match the precession frequency ω_0 being able to reach resonance in the tissues. Secondly, gradients in the magnetic fields need to be present to distinguish slices within the tissues. This leads to a range of different resonance frequencies throughout the whole tissue. This range of frequencies is simply acquired by applying a gradient in the \hat{z} -direction as

$$B_z = B_0 \pm \Delta B, \quad (2.4)$$

where ΔB is the change in the field along the z -axis. This leads to a change in

resonance frequency for each position on this axis, given by the Larmor equation in (2.1). Using slightly different frequencies of the RF pulse, it is possible to carefully select a slice of interest in the medium. Furthermore, the spatial information needs to be found in the xy -plane. This is achieved by again applying a gradient on the B_1 field, similar to the B_0 . This idea of using gradients to map the position of spins is called spatial encoding, and the contribution of the RF frequency and phase needs to be considered.^[2] The spatial encoding can be properly designed by carefully selecting the gradients in all directions.

Additionally, the FID needs to be measured and sampled properly. There are two orthogonally arranged coils, configured in quadrature. One measures the in-phase component, which corresponds to the real part of the signal, while the other measures the quadrature component, corresponding to the imaginary part. This implies that each measurement will have a signal on the form $A \cdot e^{-ix}$. The measurements are arranged in a matrix which is in the reciprocal space. Filling this space, normally phrased as filling the k -space, will occur using the FID signals within each voxel. The process is depicted in figure 2.4.1.

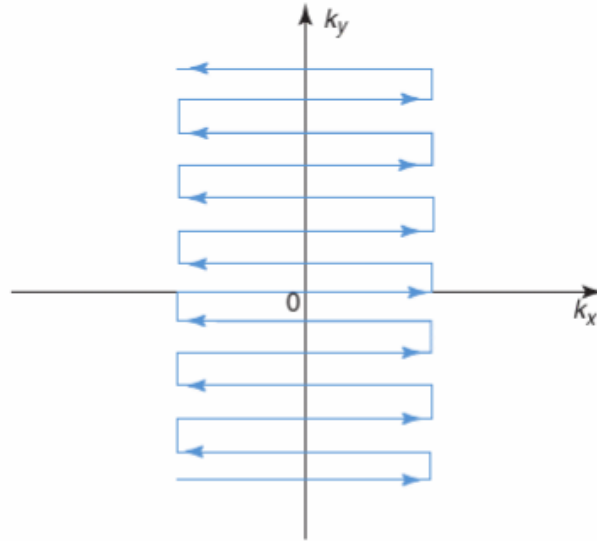


Figure 2.4.1: Filling the k -space with the real and imaginary parts from the FID signal. Adopted from [2].

Finally, when the k -space is filled, the Fourier inverse transform can be utilized to create an image of a slice. The quality in terms of resolution, field of view (FOV), signal-to-noise ratio (SNR), and contrast-to-noise ratio (CNR) will be highly dependent on all the technical details and variables such as magnetic

field strength B_0 , gradient ΔB , and the repetition and echo times T_R and T_E . Considering all of this, high-quality and useful MRI scans can be acquired.

2.5 Chemical Shift

Until now, it has been assumed that the ^1H protons resonates at the same frequency given by the Larmor equation. The signals from different tissues, e.g. water and fat, do, however, not arise from the same resonance frequency. This effect, caused by the chemical environment of nucleus and electrons, is called shielding and makes the ^1H experience a slightly different magnetic field.^[7] This local change in the field leads to a shift in frequency and, hence, a distinct peak in the MRS signal for individual ^1H . Delving into the Larmor equation, this shifted frequency depends on B_0 and will cause a transposed resonance.

Furthermore, this shift also depends on the magnetic field strength, where it is larger on a 7T scanner than on a 3T. Introducing the chemical shift, δ , given in ppm, the relative shift of the ^1H can be described independently of the B_0 strength. Given a 7T scanner, the resonance frequency is

$$\omega_0 = \gamma \cdot B_0 = 42.58 \frac{\text{MHz}}{\text{T}} \cdot 7\text{T} \simeq 298\text{MHz}, \quad (2.5)$$

which yields a 298 Hz shift in resonance frequency of a metabolite at 1 ppm. The metabolite glutamate, with a chemical shift of 3 ppm, has, consequently, a shift of 894 Hz that needs to be considered, driving it into resonance.

Introcuotion to Chemical Exchange Saturation Transfer

CEST is a novel NMR technique that allows non-invasive imaging of low-concentrated metabolites in tissues. The concentrations of some important metabolites are too low, making it challenging to reach a detectable signal. This problem can be solved using molecular information of the metabolites in resonance. During resonance, ^1H will exchange between molecules, characterized by the exchange rate k_{ex} . By exciting ^1H in the low-concentrated pool of metabolites, they will, after some time, change their place with surrounding water molecules. This leads to a decreased water signal due to the excited ^1H in H_2O . CEST is thus an indirect measure of compounds, measuring water that reflects the amount of low-concentrated metabolites. The principle of CEST is illustrated in figure 2.5.1.

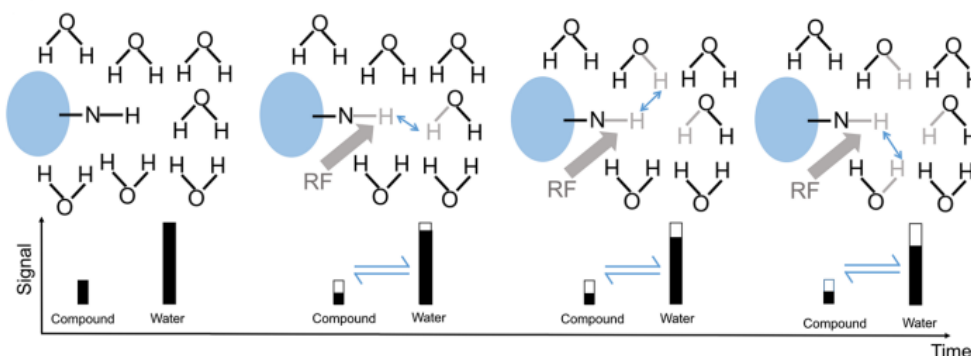


Figure 2.5.1: The basic idea of CEST. ^1H bounded to the compound (blue shape) exchange with its neighboring hydrogens given by the exchange rate k_{ex} . This chemical exchange will, after some time, be saturated and the reduction in the water signal can be measured to indirectly measure the concentration of the compound. Adopted from Wu et al. (2016).

The final product of using CEST MRI is a heatmap where all the regions of low-concentrated metabolites are highlighted. This is normally superimposed on a regular MRI scan to provide the exact localization of the compounds.

2.6 Adding Molecular Information to MRI

Imaging of low-concentrated metabolites with CEST utilizes MRS. Knowing at what frequency different metabolites are resonating, it is possible to excite only those of interest. An MRS spectrum of some important metabolites is shown in figure 2.6.1.

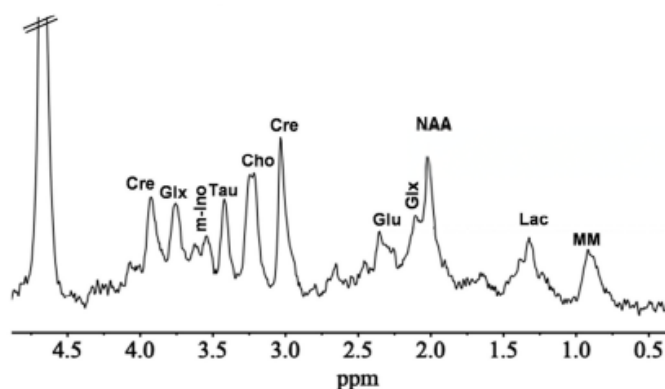


Figure 2.6.1: A MRS spectrum of different metabolites in the brain. The spikes are each metabolite's chemical shift given in ppm. Adopted from Soni et al. (2024).

The values on the x -axis are given in ppm as described in section 2.5. The chemical shift is defined

$$\delta \text{ [ppm]} = \frac{\omega_0 - \omega_{ref}}{\omega_{ref}} \cdot 10^6, \quad (2.6)$$

where ω_0 is the Larmor frequency of the compound of interest, and ω_{ref} is the reference frequency used for defining 0 ppm. Measuring the water signal under saturation for different δ , also called frequency offsets, will sequentially provide the Z-spectrum, Z_{sat} . This spectrum exhibits the CEST signal for different frequency offsets, normally between 5 and -5 ppm, where it measures the magnetization transfer ratio (MTR). Z_{sat} is normalized by an unsaturated scan Z_0 “far” away from the exchange regime, normally at -100 or -300 ppm, which yields the final $Z = \frac{Z_{sat}}{Z_0}$. Z-spectrums for different pH in a GluCEST study are shown in figure 2.6.2.

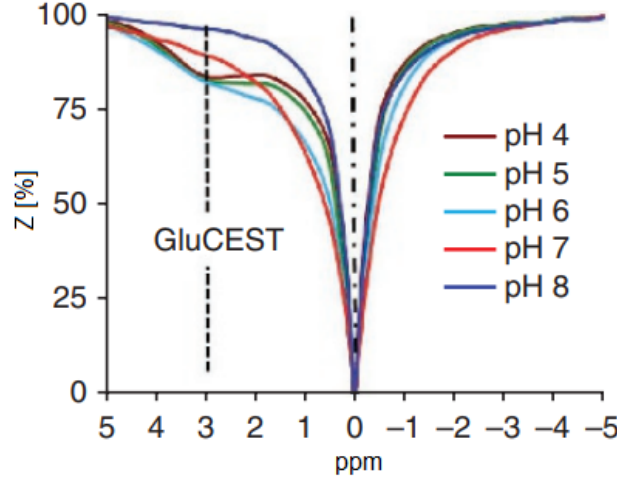


Figure 2.6.2: An example of the Z-spectrum for glutamate with different pH. The GluCEST effect, with a reduction in water signal, is found at 3 ppm. Adopted from Cai et al. (2012).

On the left-hand side, where δ is greater than 0 ppm, exchanging ^1H between metabolites and water will occur. Owing to this, the water signal at those frequencies decreases. For glutamate, which we know resonates at 3 ppm, the spectrum will show a dip due to the reduction in the water signal. Assuming that the direct water saturation (DS), i.e. the saturated water signal, is symmetrical around 0 ppm, we can calculate the difference between the value at -3 ppm and 3 ppm. This difference reflects the change in water signal, and hence, how much glutamate there is present. This difference, caused by the asymmetry, is calculated as the asymmetric magnetization transfer ratio (MTR_{asym}) as

$$\text{MTR}_{\text{asym}} = \text{MTR}(-\delta) - \text{MTR}(+\delta) = Z(-\delta) - Z(+\delta) \quad (2.7)$$

This quantity reveals the relative amount of the metabolites within a voxel. MTR_{asym} measurements for several voxels in a slice lead to a heatmap describing the metabolism and localization of the metabolites.

2.7 Controlled CEST Sequences

The sequences for CEST need to be meticulously set up. It is bounded by the pulse shape, RF saturation time, pulse power, and exchange rate, among other variables. Furthermore, the number of pulses during the saturation must be determined to drive the exchanging ^1H into saturation. This is accomplished in the RF saturation time with several pulses with pulse lengths t_p . The three steps in the pulsed CEST setup are shown in figure 2.7.1.

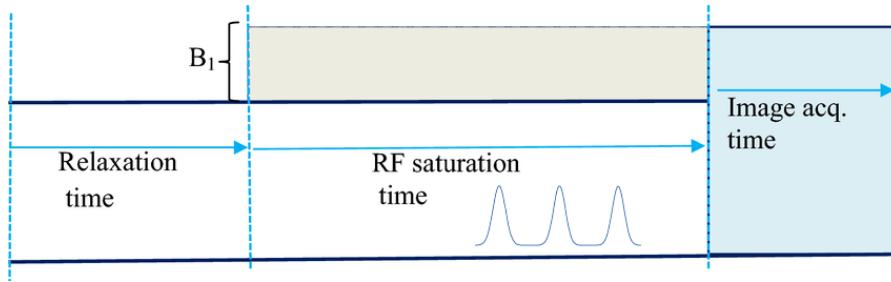


Figure 2.7.1: The three steps in the CEST setup. During the RF saturation time, pulses with period t_p cause the exchange of ^1H . Adopted from Simegn et al. (2020).

The first phase of relaxation eliminates the previous CEST effect, ensuring that each saturation contributes independently. The pulses in the second phase drive the exchange into saturation, while the third phase acquires the image. The saturation pulses may be chosen task-specific, in varieties of gaussian-, sinc-, or binomial pulses, etc.

Some trade-offs need to be considered while designing the pulse sequence: A larger number of pulses will saturate the exchange of ^1H . At the same time, it will be a cost in time. Similarly, a trade-off in pulse power will affect the number of ^1H in exchange. Powered pulses that are too low will not saturate the protons sufficiently, while pulses with too high power will saturate too many ^1H . Both extrema will, in effect, lead to a lower CEST signal. As a result, all these introduced quantities need to be considered to obtain a controlled CEST sequence and later a CEST image.

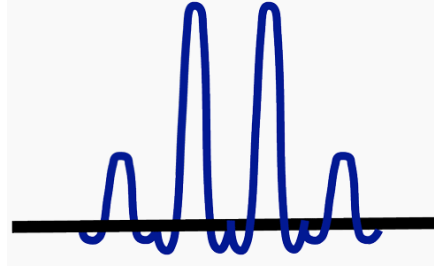


Figure 2.7.2: An example of a binomial saturation pulse. Along with shapes like gaussian and sinc, the pulses are designed to excite ^1H so they exchange with their neighboring ^1H . Adopted from [8].

2.8 Fitting the Z-spectrum

The B_0 field is created by large magnets and cooled down to less than 4 K for conducting reasons. Hence, for the sake of hardware constraints, there are inhomogeneities in the magnetic field inside the scanner. This error can be reduced by shimming.^[2] Shimming is a technique that accounts for the B_0 inhomogeneities by measuring the inhomogeneities before each scan. This measure can then be used to correct the errors. There will, however, always be challenges while sampling the Z-spectrum due to spatial and temporal fluctuations in the B_0 . Thus, a Z-spectrum calibration is needed.

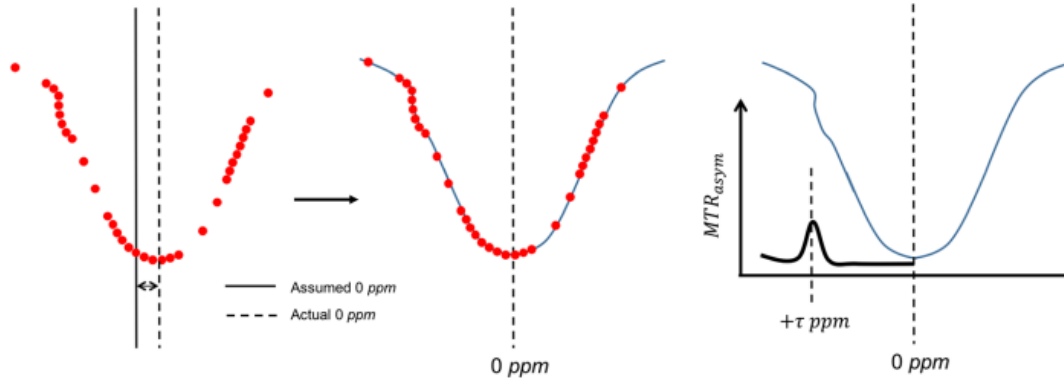


Figure 2.8.1: Calibration of the Z-spectrum. By interpolating the samples concerning the B_0 inhomogeneities, the spectrum can be calibrated. Adopted from Wu et al. (2016).

The errors in the B_0 can be counted for using interpolation. Knowing that the DS should be symmetrical around 0 ppm, the Z-spectrum can be shifted, i.e. interpolated, to localize the minima at 0 ppm. This calibration is a key step in reaching a reliable CEST image. Finally, the MTR_{asym} can be calculated for each voxel, within a slice, and mustered as a CEST image.

2.9 Artifacts in MRI

Ultimately, the CEST MRI protocol for acquiring the images needs to be considered to mitigate the types of artifacts that can arise. A common artifact is the *Gibbs artifacts*, or *ringing artifacts*, which is challenged by poor sampling in Fourier calculations. This originates from ripple effects in not ideally square waves, making the pixel values alternate around their true value. This can in some cases lead to stripes, lines, or circles in the MRI scan.

Another usual artifact can occur when T_R and T_E are poorly chosen. If their relation is such that the readout happens too early or too late, or that the inversion pulse, i.e., the 180° pulse, is improperly timed, the magnitude of \vec{M} will not represent its true state. This will in effect lead to a wrong representation of the tissues and samples in the scanner.

Artifacts of a previously made phantom with only two NMR tubes are shown in figure 2.9.1 and 2.9.2. In the right image, the relation of T_R and T_E does not fit, resulting in misrepresentation of the pixels.

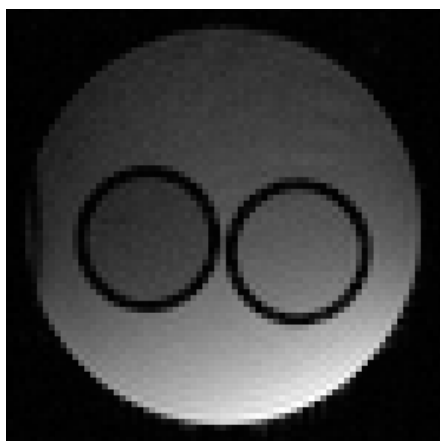


Figure 2.9.1: Image with $T_R=5$ ms and $T_E=2.5$ ms.

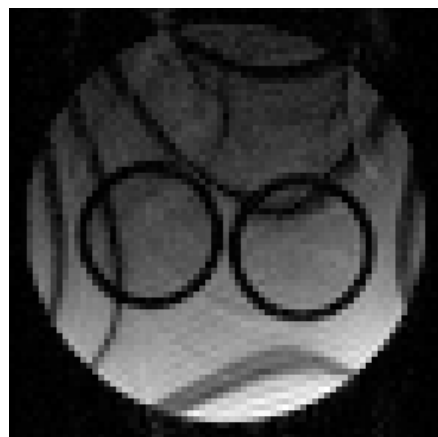


Figure 2.9.2: Image with $T_R=30$ ms and $T_E=15$ ms.

GluCEST imaging data were acquired using a 7T pre-clinical scanner (Bruker BioSpec, ParaVision 6.0.1) with an 86 mm volume coil. Phantoms used for the acquisitions were glutamic acid in phosphate-buffered saline water (PBS). Six NMR tubes of ranging glutamate concentrations were placed circularly inside a larger transportation tube. The pulse sequences implemented on the 7T Bruker scanner are designed and developed at *AD Anderson Cancer Center* (Texas, U.S.) by Mark D. Pagel. GluCEST data were acquired at 51 frequency offsets and GluCEST images were post-processed in Python.

3.1 Phantom preparation

Glutamic acid in PBS was prepared with different concentrations ranging from 2 mM to 10 mM. The pH value was adjusted to 7 with HCl (0.1 M) and NaOH (2 M). 10 and 8 mM solutions were prepared and diluted to 6, 4, and 2 mM concentrations. In addition to glutamic acid solutions, PBS (0 mM) was included as a reference, as detailed in table 3.1.1.

Table 3.1.1: Glutamic acid solutions in NMR tubes with pH adjusted to 7.

NMR tube	Concentration [mM]
1	10
2	8
3	6
4	4
5	2
6	0

The NMR tubes were sealed with parafilm and tape after being filled. The tubes were arranged circularly inside a transportation tube with clockwise decreasing concentrations from 10 to 0 mM. The transportation tube is 13 cm tall and has a diameter of 27 mm. A supporting structure was designed as a disk with six holes in it to keep the NMR tubes stable and parallel. This support was designed in *TinkerCad* and 3D-printed in PLA plastic using an *Ultimaker S5* printer. The transportation tube was filled with PBS as a background so the GluCEST effect in each NMR tube would be easier to observe.



Figure 3.1.1: The phantom contained 6 NMR tubes ranging from 10 mM to 0 mM concentrations of glutamic acid. The yellow disks inside were 3D-printed for the tubes to be stable and parallel, and the space around the tubes was filled with PBS.

3.2 GluCEST experiment

The adjustable saturation pulse parameters in CEST MRI were explored to investigate the different GluCEST effect. A T_2 -weighted image was taken to localize the phantom in the scanner. It is important to position the phantom, along with the slice of interest, at the center of the scanner. In this location, the homogeneity of B_0 is optimal, resulting in the most reliable image.

The proposed CEST sequence was set with reference to Pagel^[A] and Cai et al. (2012) with 10 pulses of $t_p=300$ ms, B_1 pulse power $3 \mu T$, and 50 frequency offsets from 5 ppm to -5 ppm. An unsaturated scan at -100 ppm was used for normalization. This saturation time of 3 s was used as a baseline for the research. Pulses with deviation from the baseline were explored as specified in table 3.2.1.

Table 3.2.1: Details of the CEST sequences. The last acquisition marked with * was acquired with B_0 shimming inside the container.

Acquisition	Pulse length [ms]	Pulse power [μ T]
1	300	3
2	200	3
3	300	2
4	300	4
5	100	3
6*	300	2

The step size in the range of frequency offsets was 0.2 ppm. This is a time-consuming number of offsets, but it will, in turn, sample the Z-spectrum more densely and allow flexible post-processing. The resonance frequency for glutamate is around 3 ppm, making the proposed range from 5 ppm to -5 ppm acceptable. The GluCEST images were acquired with an in-plane pixel size of $313 \mu\text{m} \times 313 \mu\text{m}$ (matrix size = 128×128 , FOV = $20 \text{ mm} \times 20 \text{ mm}$) with a slice thickness of 5 mm.

The saturation pulses utilized in the sequences from Pagel consisted of a series of binomial pulses, as shown in figure 2.7.2. For each frequency offset, pulses cause the ^1H to exchange in 3 s. The interpulse delay between each binomial pulse was 0.01 ms. The readout acquisition method for all images was *Fast Imaging with Steady-State Precession* (FISP). FISP was used after the saturation pulse to read the signal efficiently, hence “Fast Imaging”. Post-processing of the raw data leads to CEST images, where GluCEST effects can be observed.

3.3 Post-processing

All images were stored in a *Digital Imaging and Communications in Medicine* (DICOM) format, containing information about the phantom used in the acquisition procedure. A Python script^[A] read the DICOMs, used the PyDicom^[9] and PyPulseq^[A] libraries, and calculated the Z-spectrum for each CEST acquisition. A snippet from the code reveals how the sequence and offset information were read and stored for later calculations.

```
data = pydicom.dcmread(data_path)
seq = pypulseq.Sequence()
seq.read(seq_path)
```

```
m0_offset = seq.get_definition("M0_offset")
offsets = seq.get_definition("offsets_ppm")
```

The Z-spectrum was finally obtained by extracting the data as m_z , representing the magnetization in \hat{z} -direction, and normalized by the reference scan at -100 ppm, denoted $M0$ in the script. The following snippet lists the procedure of normalization.

```
M0_idx = np.where(abs(offsets) >= abs(m0_offset))[0]
if len(M0_idx) > 0:
    M0 = np.mean(m_z[M0_idx, :], 0)
    offsets = np.delete(offsets, M0_idx)
    m_z = np.delete(m_z, M0_idx, axis=0)
    Z = m_z / M0
```

The normalized Z-spectrum, Z , was further calibrated using smoothing spline interpolation.^[A] The spectrum for each pixel was effectively shifted such that the minima was at 0 ppm. Finally, the MTR_{asym} was calculated around 3 ppm as in equation (2.7). The region of interest (ROI) used to calculate the MTR_{asym} values for each concentration is a fitted matrix of shape 9x9 that covers as much as feasible within each NMR tube. One selected pixel of this ROI is utilized to generate the Z-spectrums and MTR_{asym} spectrums.

Results of the GluCEST MRI

Several acquisitions were conducted to investigate the GluCEST effect that leads to contrast enhancement. Pulse design of the GluCEST sequences includes several variables, as elaborated in chapter 2, and their duration and power were explored. GluCEST measurements of the phantom, containing six NMR tubes with concentrations ranging from 10 mM to 0 mM, were analyzed and post-processed. Images were obtained as depicted in chapter 3. A T_2 -weighted localizer scan was obtained to determine the position within the scanner, and the Z-spectrums and the MTR_{asym} spectrums were calculated and shown together with their corresponding heatmaps.

4.1 GluCEST contrast enhancement

A T_2 -weighted (T2W) localizer image was acquired to verify the position of the phantom. It should be placed close to the bore center of the scanner where B_0 has the least inhomogeneities. The T2W image is shown in figure 4.1.1.

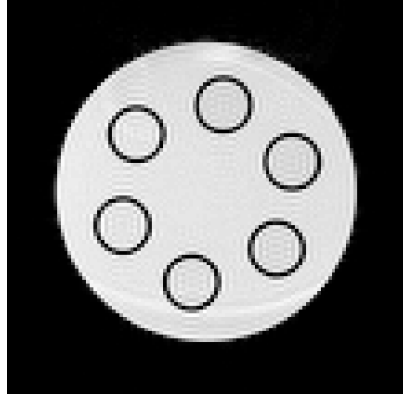


Figure 4.1.1: A T_2 -weighted image was acquired to adjust the positioning of the phantom inside the scanner.

A normalized B_0 map is obtained and visualized in figure 4.1.2 to observe the spatial inhomogeneities within the scanner. The lower part of the phantom experiences a slightly lower magnetic field than the rest, which, in turn, leads to lower precession frequencies of the ^1H protons and inaccurate readouts.

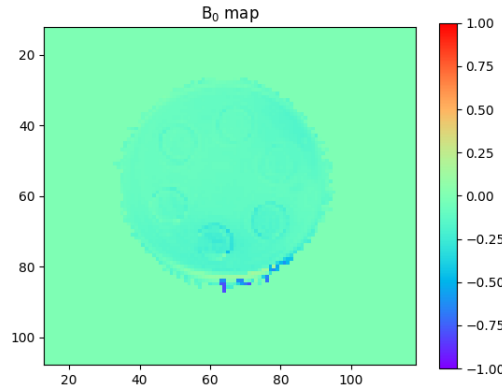


Figure 4.1.2: A B_0 map revealing the spatial inhomogeneity of the B_0 field within the scanner.

The GluCEST protocols employed to acquire the results are elaborated in chapter 3, and each acquisition is detailed in table 3.2.1. The Z-spectrums, MTR_{asym} spectrums, and the GluCEST images for $\delta=3.00$ ppm are shown below.

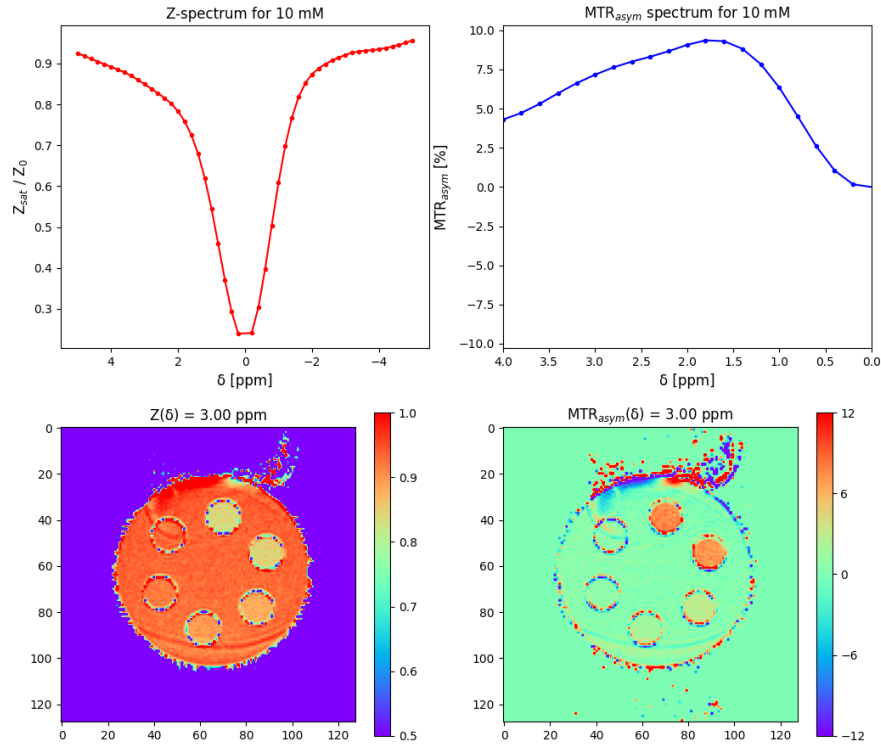


Figure 4.1.3: Acquisition 1. The GluCEST imaging was obtained with $t_p=300$ ms and $B_1=3 \mu T$ and used as a baseline.

Table 4.1.1: MTR_{asym} of different concentration glutamic solutions for acquisition 1.

Glutamic Acid Concentration [mM]	MTR_{asym} [%] (mean \pm SEM)
10	7.54 ± 0.08
8	7.12 ± 0.07
6	2.83 ± 0.08
4	1.65 ± 0.08
2	0.76 ± 0.06
0	1.06 ± 0.24

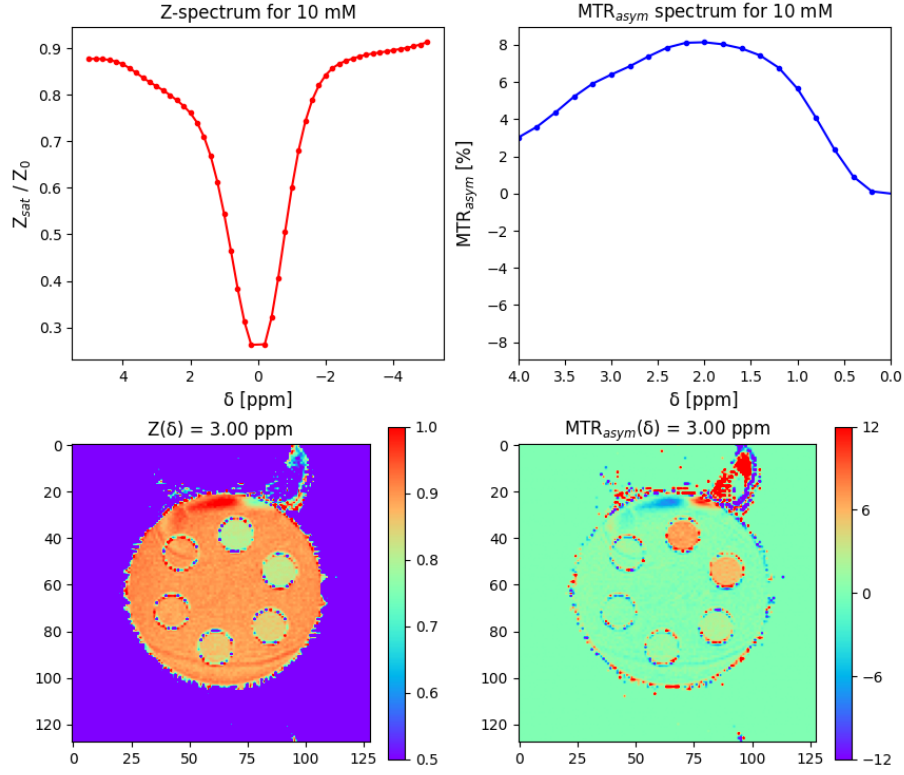


Figure 4.1.4: Acquisition 2. The GluCEST imaging was obtained with $t_p=200$ ms and $B_1=3 \mu T$.

Table 4.1.2: MTR_{asymp} of different concentration glutamic solutions for acquisition 2.

Glutamic Acid Concentration [mM]	MTR_{asymp} [%] (mean \pm SEM)
10	6.77 ± 0.06
8	5.68 ± 0.06
6	2.13 ± 0.06
4	0.98 ± 0.08
2	0.55 ± 0.06
0	0.87 ± 0.14

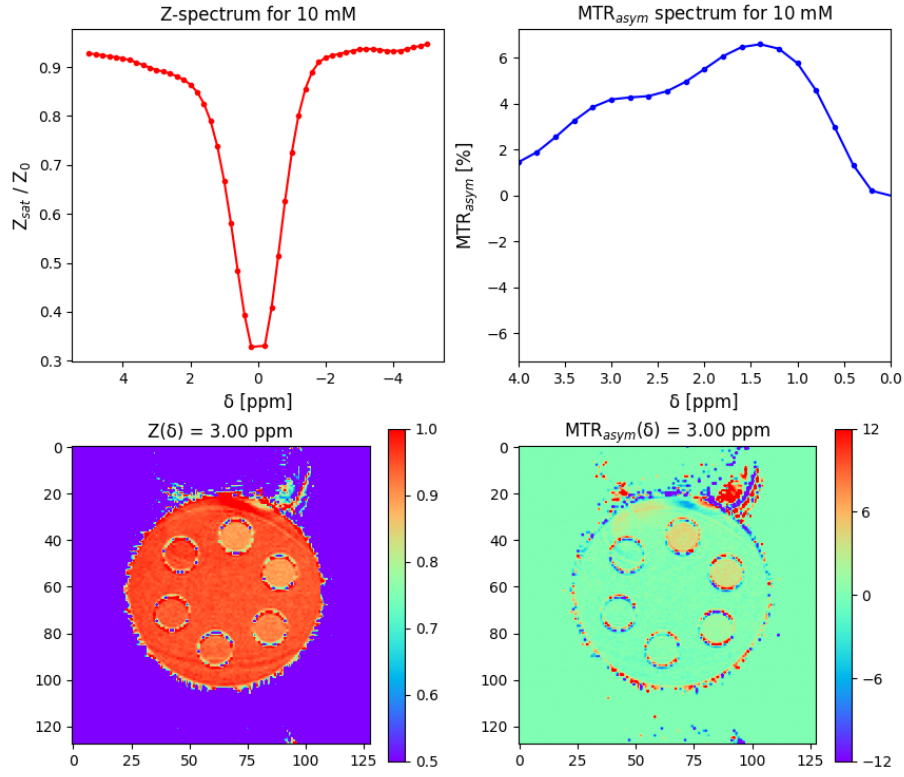


Figure 4.1.5: Acquisition 3. The GluCEST imaging was obtained with $t_p=300$ ms and $B_1=2 \mu T$.

Table 4.1.3: MTR_{asym} of different concentration glutamic solutions for acquisition 3.

Glutamic Acid Concentration [mM]	MTR_{asym} [%] (mean \pm SEM)
10	4.15 ± 0.07
8	3.60 ± 0.08
6	1.32 ± 0.06
4	0.31 ± 0.07
2	0.10 ± 0.06
0	-0.20 ± 0.14

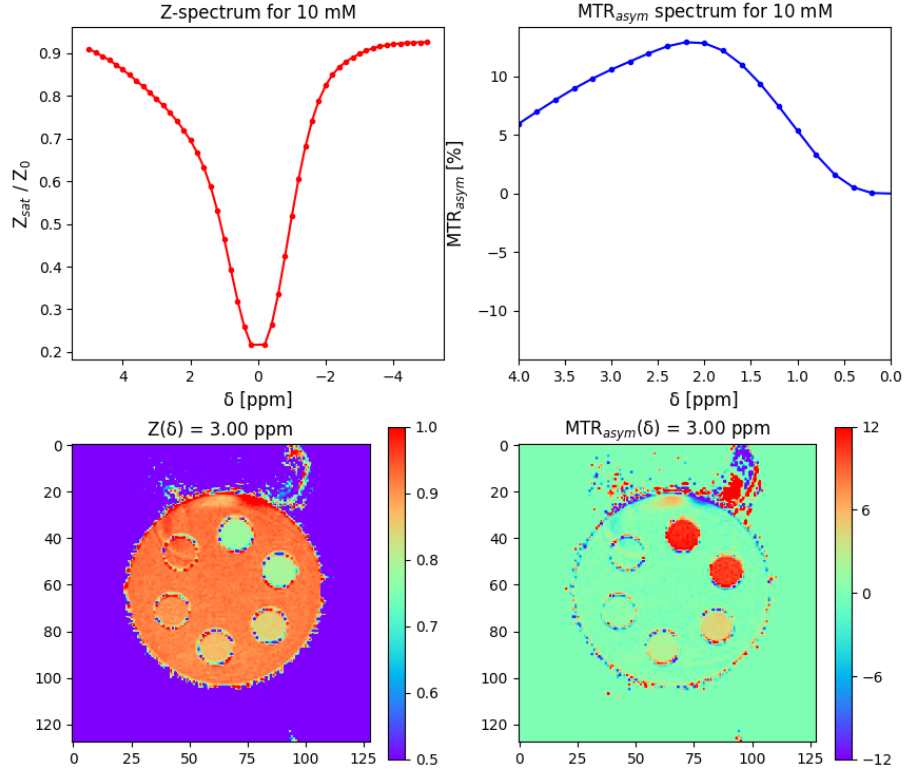


Figure 4.1.6: Acquisition 4. The GluCEST imaging was obtained with $t_p=300$ ms and $B_1=4 \mu T$.

Table 4.1.4: MTR_{asym} of different concentration glutamic solutions for acquisition 4.

Glutamic Acid Concentration [mM]	MTR_{asym} [%] (mean \pm SEM)
10	10.79 ± 0.08
8	10.14 ± 0.07
6	4.47 ± 0.06
4	2.24 ± 0.07
2	0.59 ± 0.05
0	0.41 ± 0.15

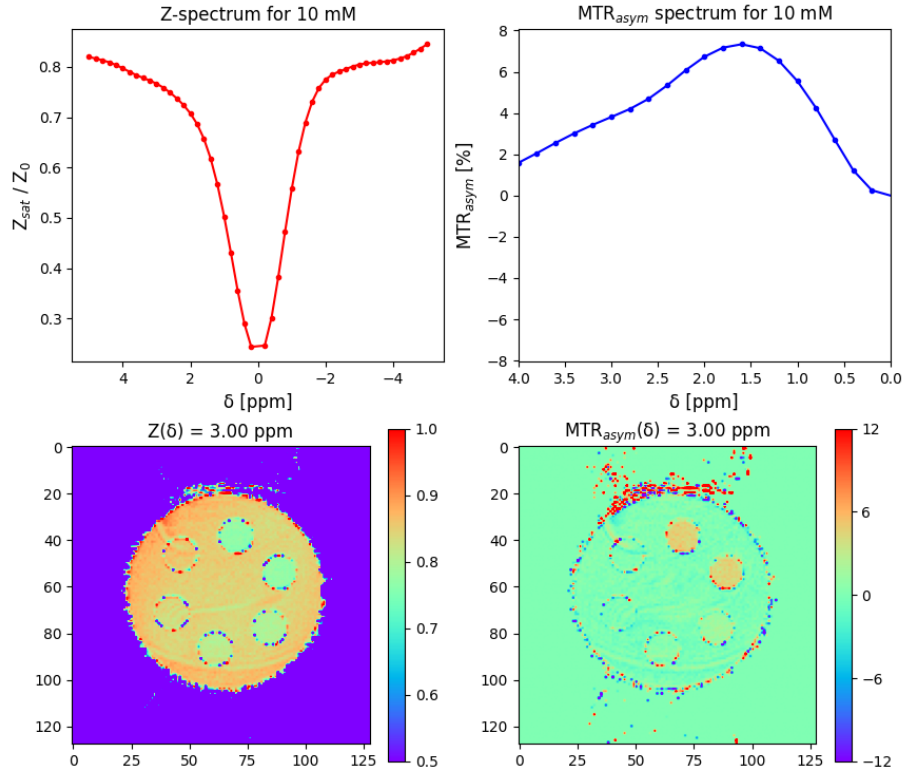


Figure 4.1.7: Acquisition 5. The GluCEST imaging was obtained with $t_p=100$ ms and $B_1=3 \mu T$.

Table 4.1.5: MTR_{asym} of different concentration glutamic solutions for acquisition 5.

Glutamic Acid Concentration [mM]	MTR_{asym} [%] (mean \pm SEM)
10	4.60 ± 0.06
8	4.31 ± 0.07
6	1.56 ± 0.06
4	0.55 ± 0.08
2	-0.15 ± 0.09
0	-0.08 ± 0.14

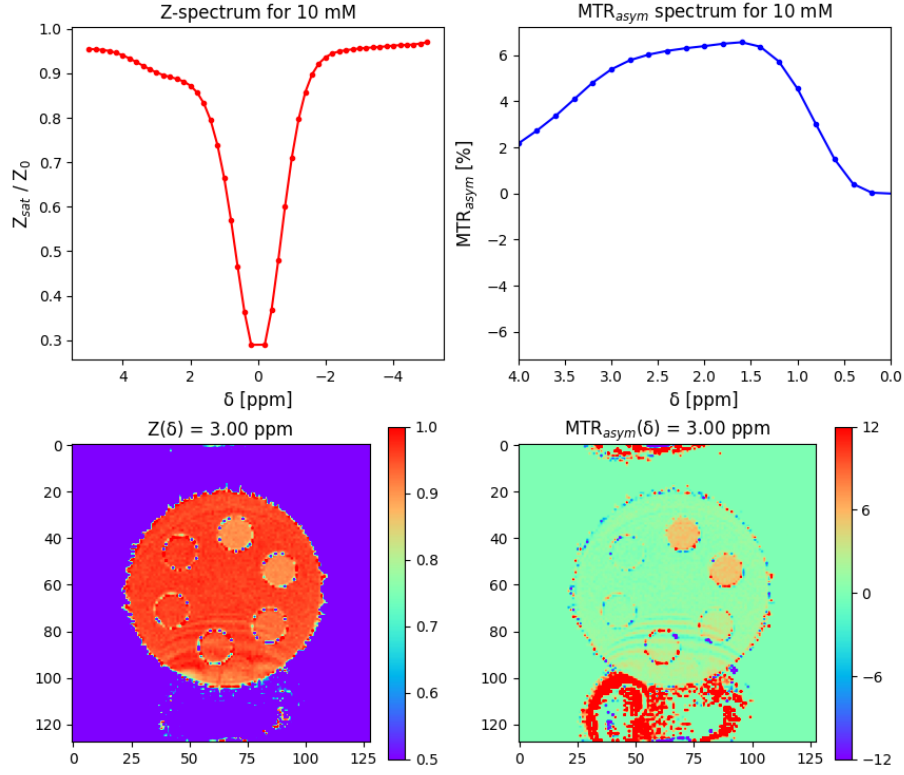
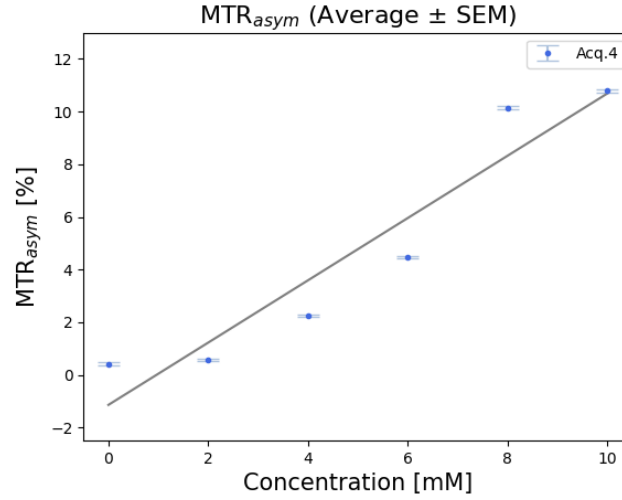


Figure 4.1.8: Acquisition 6* with shimming. The GluCEST imaging was obtained with $t_p=300$ ms and $B_1=2 \mu T$.

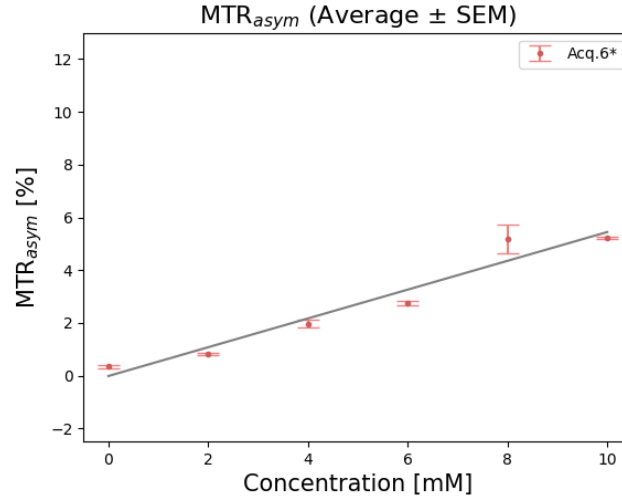
Table 4.1.6: MTR_{asymp} of different concentration glutamic solutions for acquisition 6*.

Glutamic Acid Concentration [mM]	MTR_{asymp} [%] (mean \pm SEM)
10	5.22 ± 0.06
8	5.17 ± 0.05
6	2.76 ± 0.09
4	1.97 ± 0.14
2	0.83 ± 0.05
0	0.34 ± 0.05

It is clear that the glutamic acid solutions of higher concentrations were associated with a higher CEST effect, and, accordingly, that the visual clockwise gradients of MTR_{asym} are observed with a reduction of concentration. Differences between each acquisition were apparent, with the highest contrast resulting from the increased B_1 power of $4 \mu T$ and the lowest contrast from the reduced saturation time of 1 s, with $t_p=100$ ms. The linear dependency of MTR_{asym} on glutamic acid concentrations in acquisition 4 and 6* are shown in figure 4.1.9.



(a) Acquisition 4.



(b) Acquisition 6*.

Figure 4.1.9: The dependence of GluCEST effect on glutamic acid concentrations. (a) $t_p=300\text{ms}$ and $B_1=4\mu T$. (b) $t_p=300\text{ms}$ and $B_1=2\mu T$ with shimming. The fitted lines show the linear dependence of GluCEST effect on Glu concentrations.

4.2 Artifacts

Regions of miscalculated GluCEST effects can be observed in the images due to MRI artifacts. In some images, unwanted effects occurred in the 0 mM tube, and noise was present in the central upper and lower parts of all images. Moreover, in acquisition 6*, there was a wrap-around artifact where structures in the image were shifted downwards and repeated at the top. The former artifacts arose from inhomogeneities in the B_0 field and Gibbs artifacts, while the latter was due to aliasing.

Poor results from artifacts were seen in table 4.1.5 for the baseline measurement. Here, the MTR_{asym} of the 0 mM concentration was higher than the solution of 2 mM. This was a direct result of the occurrence of Gibbs artifacts in the 0 mM tube.

The results indicated that increased pulse powers and longer saturation times induce an increased GluCEST effect in Glu-phantoms (glutamic acid solutions). Additionally, the linear dependence of MTR_{asym} at 3 ppm on Glu concentrations alludes that glutamate can be quantitatively imaged using GluCEST MRI.

5.1 GluCEST contrast variations

The linear dependence of GluCEST effect on glutamate concentrations was consistent through all scans, as demonstrated by two representative acquisitions in figure 4.1.9. Glutamate solutions with the highest concentrations exhibited the highest effects, especially for 10 and 8 mM. The range of this linear dependency of GluCEST on concentrations can be further explored beyond 10 mM, within the physiological and pathological glutamate concentration range.

All acquisitions resulted in a reduced MTR for positive frequency offsets due to the exchange of glutamate on these frequencies. There are, however, other frequencies than 3 ppm that contribute to GluCEST signals. A broad CEST effect causes the Z-spectrum from 5 to 0 ppm to be reduced. In the GluCEST image with the highest MTR_{asym} , i.e. in acquisition 4, this broad downfield of the positive side of the frequency range can be observed. The decay leads to a higher MTR_{asym} due to the asymmetry in the Z-spectrum. This broad CEST of glutamate at pH 7 ranging from 1 to 4 ppm was reported by Cai et al. (2012) due to the phenomenon of intermediate- to fast-exchange ($k_{\text{ex}} \geq \Delta\omega$)-mediated chemical shift averaging. Acquisition 6* reveals a sharper downfield peak at 3 ppm, showing promise for achieving GluCEST effects at this frequency alone.

This linear proportional dependence of MTR on Glu concentrations is clear. Among the performed acquisitions, acquisition 4 with the highest saturation

power of 4 uT and 3 s saturation time, yielded the largest GluCEST effect at 3 ppm.

Interestingly, by using shimming in acquisition 6*, the linearity of GluCEST effect seemed to hold with increased concentration. This linearity can be seen in figure 4.1.9. For acquisition 4, where the pulse power is increased, the regression line deviates more. This results in a less optimal search of glutamate, even though the contrast appears promising.

There are boundaries for the saturation transfer to occur, where pulse design needs special attention while being implemented. As detailed in chapter 4, the strongest B_1 pulsed raised the highest contrast. This does not necessarily mean that GluCEST effect always benefits from increased pulse power as the magnetization transfer effects depend strongly on the B_1 (Völzke et al. 2024). Very strong B_1 fields can cause more ^1H to exchange than desired, while weak fields will not give rise to sufficient chemical exchange. Similarly, when applying pulses with long saturation times, the exchange processes can be overwhelmed, resulting in weaker CEST signals. This additive time is time-consuming, especially when the number of offsets increases. It is, hence, reasonable to simulate the exchange processes for different pulse powers and saturation times to see how their effects contribute. For this to be done properly, the Bloch matrix system introduced in chapter 2 needs to be considered.

In light of quantitatively measuring glutamate, varieties of glutamate concentrations are used. The results are similar for all acquisitions: The GluCEST effects increase with glutamate concentration.

5.2 Future work

Several variables can be further explored to verify the reliability of GluCEST and enhance the image contrast. Zaiß et al. (2022) did so by varying the B_0 and B_1 fields and observe their affection to water pools. Another group did a comprehensive 7T CEST for clinical use, covering the exchange rate regimes of metabolites (Fabian et al. 2023). Stilianu et al. (2024) have designed new pulse shapes to improve the image contrast, while a novel approach for faster acquisition has been made by Völzke et al. (2024). Exploring the impact of different variables, such as B_1 , k_{ex} , and pulse shapes, in combination can lead to a more robust and comprehensive method. Similar attempts to those mentioned need to be investigated, tested, and integrated to enhance the mapping of neurometabolism.

The next stage of the study will consist of one of two possible options. The first is to keep working on the pre-clinical pipeline, and, additionally, include MRS

and MALDI mass spectroscopy imaging (MALDI-MSI) to add spectroscopic information. This can provide another indication of whether the GluCEST reflects the concentrations of glutamate or not. The other possible option is to move towards clinical application and post-processing. Here, it is possible to use acquired data from healthy volunteers and compare post-processing pipelines of different research groups, e.g. from universities in Bonn, Erlangen, and Pennsylvania.

Conclusion

The study shows that the provided chemical exchange saturation transfer (CEST) magnetic resonance imaging (MRI) protocol is a promising tool for mapping the neurometabolite glutamate to investigate early changes in neurodegenerative disorders. Contrast enhancement in glutamate-weighted CEST (GluCEST) has been explored using different saturation times and pulse powers *in vitro* of phantoms of varied glutamate concentrations.

The strongest GluCEST effect achieved was with 3 s saturation time and $2 \mu T$ pulse power, which yielded an $MTR_{\text{asym}} = 5.22 \pm 0.06 \%$ in the 10 mM glutamate solution. In this acquisition, there was a linear dependence of GluCEST effects on increased concentration from 0 mM to 10 mM. The acquisition with the highest contrast, achieved with 3 s saturation and $4 \mu T$, resulted in an $MTR_{\text{asym}} = 10.79 \pm 0.08 \%$, yet simultaneously exhibited poorer linearity.

The proposed GluCEST MRI demonstrated a linear dependence on Glu concentration, and the image acquisition enables quantitative mapping of concentrations in phantoms.

Bibliography

- Cai, K. et al. (2012). “Magnetic resonance imaging of glutamate”. In: *Nature Medicine*. DOI: [10.1038/nm.2615](https://doi.org/10.1038/nm.2615).
- Fabian, M. et al. (2023). “Comprehensive 7 T CEST: A clinical MRI protocol covering multiple exchange rate regimes”. In: *NMR in Biomedicine*. DOI: [10.1002/nbm.5096](https://doi.org/10.1002/nbm.5096).
- Simegn, G. et al. (2020). “Chemical Exchange Saturation Transfer MRI Optimal Continuous Wave RF Irradiation Parameters for Glycogen (glycoCEST) Detection”. In: *Magnetic Resonance*. DOI: [10.1007/s00723-020-01208-y](https://doi.org/10.1007/s00723-020-01208-y).
- Soni, N. et al. (2024). “Detection of sex-specific glutamate changes in subregions of hippocampus in an early-stage Alzheimer’s disease mouse model using GluCEST MRI”. In: *The Journal of the Alzheimer’s Association*. DOI: [10.1002/alz.14190](https://doi.org/10.1002/alz.14190).
- Stilianu, C. et al. (2024). “Enhanced and robust contrast in CEST MRI: Saturation pulse shape design via optimal control”. In: *Magnetic Resonance in Medicine*. DOI: [10.1002/mrm.30164](https://doi.org/10.1002/mrm.30164).
- Völzke, Y. et al. (2024). “Calibration-free whole-brain CEST imaging at 7T with parallel transmit pulse design for saturation homogeneity utilizing universal pulses (PUSHUP)”. In: *Magnetic Resonance in Medicine*. DOI: [10.1002/mrm.30305](https://doi.org/10.1002/mrm.30305).
- Wu, B et al. (2016). “An overview of CEST MRI for non-MR physicists”. In: *EJNMMI Physics*. DOI: [10.1186/s40658-016-0155-2](https://doi.org/10.1186/s40658-016-0155-2).
- Zaib, M. et al. (2022). “Theory of chemical exchange saturation transfer MRI in the context of different magnetic fields”. In: *NMR in Biomedicine*. DOI: [10.1002/nbm.4789](https://doi.org/10.1002/nbm.4789).

Additional sources

- [1] Nyman, A. (-) *GluCEST: A translational biomarker of synaptic brain dysfunction*, NTNU grant project description
- [2] Webb, A.G. (2003) *Introduction to Biomedical Imaging*, John Wiley & Sons, Inc.
- [3] Suetens, P. (2009) *Fundamentals of medical imaging*, Cambridge University Press
- [4] Prasad, P.V., Storey, P. (2008). *Magnetic Resonance Imaging*, Molecular Biomethods Handbook. Springer Protocols Handbooks. Humana Press.
- [5] Wikipedia (2024), *Free induction decay*
https://en.wikipedia.org/wiki/Free_induction_decay
- [6] Siemens Healthcare GmbH (2015), *Magents, Spins and Resonances*
- [7] Rinck, P.A. (1993) *Magnetic Resonance in Medicine*, Blackwell Scientific Publications
- [8] MRI questions (2024), *Water Excitation Pulses*
<https://mriquestions.com/water-excitation.html#/>
- [9] Pydicom (2024), *Pydicom documentation*
<https://pydicom.github.io/pydicom/stable/index.html>

Appendices



Github repositories

All code and pulse sequences used in this paper are included in the Github repository linked below. Further explanations are given in the readme files.

A1 - CEST evaluation in Python

- https://github.com/kherz/pulseseq-cest-library/blob/master/eval-examples/MTRasym/EVAL_APTw_3T.py

A2 - PulSeq tools

- <https://github.com/kherz/pulseseq-cest-library>

A3 - Pagel, M. *CEST sequences*

- https://github.com/CAMEL-MartyPagel/acidoCEST_MRI_Matlab/blob/main/Acquisition%20Code/CEST_Pagel5_PV6.0.1/CEST_Pagel5_Instructions.pdf

B

Declaration of AI aids and -tools

Deklarasjon

Har det i utarbeidingen/utformingen/tilvirkingen av denne besvarelsen/oppgaven blitt brukt KI-baserte hjelpemidler?

Nei



Ja

Hvis nei, signer:

Hvis ja, fyll ut resten av deklarasjonsskjemaet.

Jeg tar fullt ansvar for teksten som denne deklarasjonen gjelder for. Jeg har kryssjekket kildene og dataene som kildene er basert på, og jeg forstår argumentene som presenteres. Jeg har ikke brukt kilder som jeg ikke anerkjenner som troverdige.

I arbeidet har jeg tatt i bruk følgende KI-baserte hjelpemidler:

Grammarly, Microsoft Copilot, Chat GPT

Jeg har brukt KI-baserte hjelpemidler på følgende måte (inntil 200 ord):

Jeg har brukt gratisversjonen til Grammarly for rettskriving underveis i rapportskrivningen. Den retter på ord som er skrevet feil og foreslår endringer på ord ("that" vs. "which", "their" vs. "these").

Microsoft Copilot og ChatGPT er brukt parallellt for å finne riktige ord til en kontekst og formulere setninger mer presist. Kun egne produserte setninger er brukt for omformuleringer.

Eksempler:

«Basert på en første idéutvikling brukte jeg Copilot til å skissere ulike mulige svar. Deretter brukte jeg Google Scholar for å finne kilder som kunne støtte eller avkrefte disse svarene»

«Jeg brukte ChatGPT for å oppsummere og forklare avsnitt.» / «Etter dette oppsummerte jeg resultatene og formulerte tekstavsnitt før jeg spurte ChatGPT om å forbedre tekstflyten»



Jeg er kjent med NTNUs regelverk for bruk av kunstig intelligens. Jeg har redegjort for all bruk av kunstig intelligens enten i) direkte i rapporten eller ii) i dette skjemaet.

Asbjørn Bjørkkjær / 12.12.24 / TRD
Underskrift/Dato/Sted